# Moiré quantum chemistry: Charge transfer in transition metal dichalcogenide superlattices

Yang Zhang ,[*] Noah F. Q. Yuan,[*] and Liang Fu

*Department of Physics, Massachusetts Institute of Technology, Cambridge, Massachusetts 02139, USA*

Transition metal dichalcogenide (TMD) bilayers have recently emerged as a robust and tunable moiré system for studying and designing correlated electron physics. In this Rapid Communication, by combining a large-scale first-principles calculation and continuum model approach, we provide an electronic structure theory that maps long-period TMD heterobilayer superlattices onto diatomic crystals with cations and anions. We find that the interplay between the moiré potential and Coulomb interaction leads to filling-dependent charge transfer between different moiré superlattice regions. We show that the insulating state at half filling found in recent experiments on $WSe_2/WS_2$ is a charge-transfer insulator rather than a Mott-Hubbard insulator. Our work reveals the richness of simplicity in moiré quantum chemistry.

Following the recent discovery of correlated insulators and unconventional superconductivity in twisted bilayer graphene [1,2] and trilayer graphene-hBN heterostructures [3,4], artificial moiré superlattices have emerged as a new venue for realizing and controlling correlated electron phenomena. The moiré superlattices and natural solids differ greatly in the magnitude of their characteristic length and energy. In solids, the average distance between electrons is typically comparable to atomic spacing in the order of Å and their kinetic and interaction energies are typically in the order of eV, while in moiré superlattices a mobile charge is shared by 1000–10 000 atoms so that the characteristic length and energy scales are in the order of 10 nm and 10–100 meV, respectively. Correspondingly, the quantum chemistry of natural solids involves complex intra-atomic and long-range interactions, while low-energy charge carriers in moiré superlattices only feel a long-period potential and interact with each other predominantly via the long-range Coulomb repulsion. Therefore, quantum chemistry can be simpler in moiré systems.

In twisted bilayer graphene, the emergence of strong correlation effects requires fine tuning to a magic twist angle, where the moiré energy bands become flattened [5] and sensitive to microscopic details such as lattice relaxation [6–11] and strain [12]. On the other hand, transition metal dichalcogenide (TMD) bilayers [13–16] have a much simpler moiré band structure. In TMD heterobilayers such as $WSe_2/WS_2$, the valence moiré bands are simply formed by holes moving in a periodic moiré potential. Therefore, TMD superlattices provide a robust platform to study many-body physics with a highly tunable kinetic energy and local interaction strength.

Very recently, a correlated insulating phase has been observed in $WSe_2/WS_2$ at a filling of $n = 1$ hole per moiré unit cell or half filling of the topmost valence moiré bands [15,16], and regarded as a canonical Mott-Hubbard insulator [17]. In this scenario, the topmost moiré band is well separated from the rest; its charge distribution is tightly localized near the moiré potential minima, forming a triangular lattice. At fillings $n \leqslant 1$, strong on-site Coulomb repulsion $U$ suppresses double occupancy, and the resulting correlated ground states are adequately captured by the triangular lattice Hubbard model [13].

In this Rapid Communication, we identify an alternate energy scale associated with charge transfer between regions with different local stacking configurations in the moiré superlattice. When the energy cost of charge transfer $\Delta$ is comparable to or smaller than the local Coulomb repulsion $U$, the Mott-Hubbard description becomes inadequate at fillings $n \geqslant 1$. Instead, the correlated insulator at $n = 1$ is a charge-transfer insulator [18], and doped charges at higher fillings $n > 1$ transfer to second potential minima on the moiré superlattice in order to avoid double occupancy of the primary minima. Using a large-scale first-principles calculation, we obtain the parameters $\Delta$ for various TMD heterobilayers and find that $\Delta$ in a $WSe_2/WS_2$ superlattice is comparable to the experimentally observed charge gap [15,16], whereas $U$ is much larger. We provide a theoretical description of the charge-transfer phenomenon by introducing an effective honeycomb lattice model, in which the $MM$ and $MX$ sublattices correspond to "moiré cations" and "moiré anions" where charges are locally concentrated. We note that previous works on twisted bilayer graphene have shown the interaction-induced charge redistribution within a local moiré region [19–21]. Here, the charge transfer we predict in TMD moiré superlattices takes place on the length scale of the moiré period ($\sim$10 nm) and can be directly observed by scanning tunneling spectroscopy (STS).

*Continuum model.* We consider a TMD heterobilayer such as $WSe_2/WS_2$, with $a$ ($a'$) as the lattice constant of the top (bottom) layer, and $\theta$ as the twist angle. The lattice mismatch leads to a moiré superlattice in Fig. 1, with a superlattice constant $L_M = a/\sqrt{\delta^2 + \theta^2}$ where $\delta = (a - a')/a'$. As illustrated in Fig. 2(b), the valence bands of two layers have a large band offset $\Delta E_g$, which is listed for various TMD heterobilayers

---

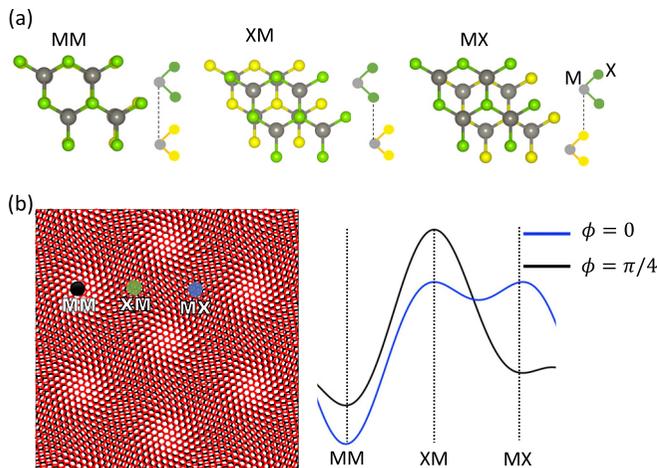*These authors contributed equally to this work.

FIG. 1. (a) Lattice structure of *MM*, *MX*, *XM* spots for *AA* stacking heterobilayer (*M* stands for metal atom and *X* stands for chalcogen atom). (b) Real-space moiré pattern of a TMD heterobilayer with $\delta = 4.0\%$, where *MM*, *MX*, *XM* spots within one supercell are labeled, and a schematic diagram for the moiré potential landscape for $\phi = 0$ and $\phi = \pi/4$, along the path from *MM* to *XM* and *MX* spots as indicated by the array in the left figure.

TABLE I. Summary of TMD heterobilayer. Here, $\delta$ is the lattice constant mismatch with respect to the bottom layer, $\Delta E_g$ is the band offset, $V_0$ and $\phi$ are parameters of the moiré potential, and $E_0^{\min} = \delta^2/(2ma^2)$ is the moiré kinetic energy at zero twist. All energies are in units of meV.

| System | $\delta$ | $\Delta E_g$ | $V_0$ | $\phi$ | $E_0^{\min}$ |
|---|---|---|---|---|---|
| WSe$_2$/WS$_2$ | 4% | 640 | 15 | 45° | 1.2 |
| WSe$_2$/MoS$_2$ | 4% | 940 | 11 | 40° | 1.2 |
| MoSe$_2$/MoS$_2$ | 4% | 630 | 9 | 42° | 1.3 |
| MoSe$_2$/WS$_2$ | 4% | 270 | 7 | 35° | 1.3 |

atom and chalcogen atom at the bottom layer, respectively.[1] There are three types of Wykoff positions in a moiré unit cell—hereafter referred to as *MM*, *XM*, *MX*, depending on the alignment of the metal atom (*M*) and chalcogen atom (*X*). As shown in Fig. 1(a), at *MM*, the metal atoms on top and bottom layers are aligned, while at *MX* (*XM*), the metal atom on the top (bottom) layer is aligned with the chalcogen atom on the bottom (top) layer.

In the long moiré wavelength limit $L_M/a \to \infty$, the valence-band maximum varies slowly over the moiré unit cell, which can be expressed as the first-order harmonics with moiré wave vectors $\boldsymbol{G}_i = \frac{4\pi}{\sqrt{3}} L_M^{-1} (\cos \frac{i2\pi}{3}, \sin \frac{i2\pi}{3})$ ($i = 1, 2, 3$) [13,22].

This is captured by the continuum model [13] $H_0 = \int \psi^\dagger(\boldsymbol{r}) \hat{\mathcal{H}} \psi(\boldsymbol{r}) d^2\boldsymbol{r}$ with

$$\hat{\mathcal{H}} = -\frac{\nabla^2}{2m} + V(\boldsymbol{r}), \tag{1}$$

$$V(\boldsymbol{r}) = -2V_0 \sum_{i=1}^{3} \cos(\boldsymbol{G}_i \cdot \boldsymbol{r} + \phi), \tag{2}$$

where $\psi^\dagger = (\psi_\uparrow^\dagger, \psi_\downarrow^\dagger)$ creates the holes and $m > 0$ is the effective mass. From a first-principles calculation with relaxed layer spacing, we find the moiré valence bands within 250 meV are formed by $\pm K$ pockets in WSe$_2$. Owing to strong Ising spin-orbit coupling at the valence-band top in WSe$_2$, spin indices are locked with valley degrees of freedom [23]. Since $\pm K$ valleys are decoupled at the long moiré wavelength limit, an effective twofold spin degeneracy arises within this low-energy model. $V_0 > 0$ and $\phi$ are the only parameters associated with the magnitude and overall phase of the three lowest Fourier components of the moiré potential [13]. When the moiré period is large, $V_0, \phi$ are intrinsic material properties independent of $L_M$, which we hereafter refer to as the moiré potential strength and moiré phase, respectively.

To obtain the values of $V_0, \phi$, we first use the large-scale density functional theory (DFT) [24,25] to calculate the moiré band structure of WSe$_2$/WS$_2$, WSe$_2$/MoS$_2$, MoSe$_2$/MoS$_2$, and MoSe$_2$/WS$_2$ at the commensurate angle $\theta = 5.68°$, as shown in Fig. 2(c). The spin-orbit coupling is included via DFT as implemented in the Vienna *ab initio* simulation package (VASP) [26]. The interaction between electrons and

at zero-twist angle in Table I. Given the large band offset, the low-energy moiré bands result from the spatial variation of the valence-band maximum of WSe$_2$ due to the lattice mismatch with WS$_2$ [22], which is described by a long-period moiré potential acting on holes in WSe$_2$.

In this work, we study TMD heterobilayers with a small twist angle starting from *AA* stacking, where the metal atom and chalcogen atom of the top layer are aligned with the metal
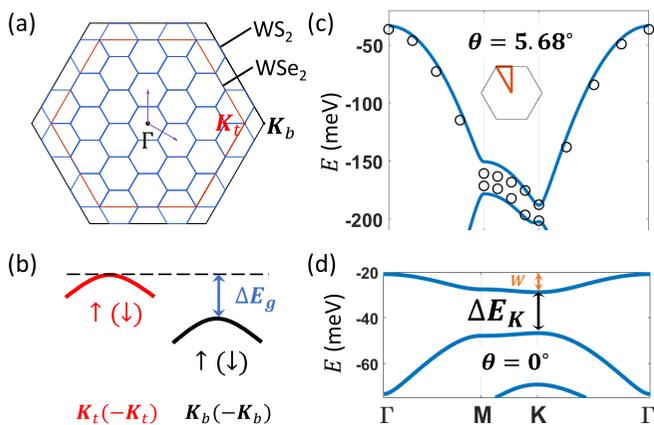


FIG. 2. (a) Brillouin zone (BZ) folding in a WSe$_2$/WS$_2$ moiré superlattice, where $a_{\text{WSe}_2}/a_{\text{WS}_2}$ is taken as 6/5 for the illustrative purpose. (b) Schematic low-energy band structure from two layers where $\pm K_{t(b)}$ are two valleys of the top (bottom) layer. (c) DFT band structure (open circle) and continuum model band structure (blue lines) at $\theta = 5.68°$. (d) Continuum model band structures of WSe$_2$/WS$_2$ at $\theta = 0°$.

---

[1] Alternatively, *AB* stacking can be viewed as a 180° rotation of the top layer.

ionic cores is approximated by the projector augmented-wave method, and the exchange-correlation potential was described by the Perdew-Burke-Ernzerhof generalized gradient approximation [27] with the van der Waals (vdW) correction incorporated by the vdW-DF (optB86) functionals [28]. We assume a rigid lattice along with in-plane directions and a relaxed interlayer distance. Depending on the different vdW correction methods, the interlayer spacing is 6.57–6.77 Å. Throughout this range of interlayer distance, we find the moiré band structure is nearly identical. At a long moiré wavelength limit, the interlayer distance has a large spatial variation [22], which affects the value of $V_0$ and $\phi$. In addition, a DFT calculation with a fully relaxed moiré superlattice would be necessary for the accurate determination of model parameters, especially around the zero-twist angle.

We find the DFT band structure fits nicely with the continuum model [see Fig. 2(c)], and obtain from this fitting the material-specific parameters $V_0$ and $\phi$ shown in Table I. For WSe$_2$/WS$_2$, $V_0 = 15$ meV and $\phi = \frac{1}{4}\pi$. Importantly, the moiré phase $\phi$ determines the energy landscape of the moiré potential. This can be seen from $V(\mathbf{r})$ at three $C_3$-symmetric points (Wyckoff positions) $\mathbf{r}_{MM} = \mathbf{0}$, $\mathbf{r}_{MX} = \frac{1}{\sqrt{3}}L_{\rm M}(1,0)$, and $\mathbf{r}_{XM} = -\mathbf{r}_{MX}$, respectively. For $0 < \phi < \frac{1}{6}\pi$, within one supercell there is one potential minimum ($MM$) and two maxima ($MX$ and $XM$), while for $\frac{1}{6}\pi < \phi < \frac{1}{3}\pi$, there are two minima ($MM$ and $MX$) and one maximum ($XM$). The four TMD heterobilayers listed in Table I, WSe$_2$/WS$_2$, WSe$_2$/MoS$_2$, MoSe$_2$/MoS$_2$, and MoSe$_2$/WS$_2$, all belong to the parameter range $\frac{1}{6}\pi < \phi < \frac{1}{3}\pi$, where the presence of two potential minima introduces different physics, as we shall show below.[2]

In the following, we will study the interaction effects in TMD heterobilayers in various regimes of $V_0$ and $\phi$. We denote $n_s = 2$ holes per supercell as the full filling and $n = \frac{1}{2}n_s = 1$ hole per supercell as the half filling.

*Charge-transfer phenomena.* In this section, we use the Hartree approximation to study the effect of the Coulomb interaction on the charge distribution in a twisted TMD heterobilayer with a relatively large bandwidth and demonstrate the charge-transfer phenomenon.

The Coulomb interaction including the background effect is

$$H_C = \int \delta\rho(\mathbf{r}) C(\mathbf{r} - \mathbf{r}') \delta\rho(\mathbf{r}') d^2\mathbf{r} d^2\mathbf{r}', \qquad (3)$$

where $\delta\rho \equiv \psi^\dagger\psi - \overline{\rho}$ is the deviation of the local hole density from the average $\overline{\rho}$ (which is set by the gate voltage), and $C(\mathbf{r}) = e^2/(4\pi\epsilon|\mathbf{r}|)$ is the Coulomb potential with a dielectric constant $\epsilon$, which controls the interaction strength. We approximate the Coulomb interaction $H_C$ by the mean-field Hatree potential $V_H$ self-consistently,

$$V_H(\mathbf{r}) = V(\mathbf{r}) + \int C(\mathbf{r} - \mathbf{r}')\langle \delta\rho(\mathbf{r}')\rangle d^2\mathbf{r}', \qquad (4)$$

and $\langle \cdots \rangle$ denotes the expectation value in the mean-field ground state. As we assume the Hartree potential preserves
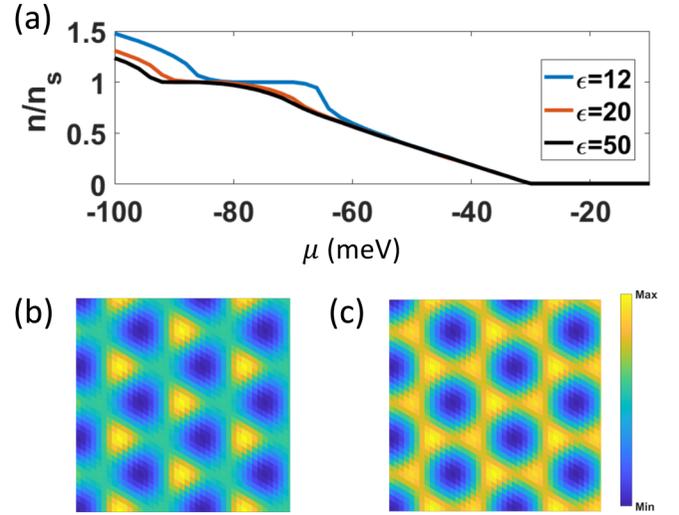
---

[2]WS$_2$/MoS$_2$ and WSe$_2$/MoSe$_2$ are discussed in the Supplemental Material [30].



FIG. 3. (a) Filling factor $n/n_s$ as a function of chemical potential $\mu$ in a WSe$_2$/WS$_2$ system at $\theta = 3°$ with $\epsilon = 12, 20, 50$. (b) and (c) are the charge distributions at half filling when $\epsilon = 50$ and 12.

all symmetries, $V_H$ can be written as a Fourier series similar to Eq. (2), and the Coulomb interaction only renormalizes the band structure [21,29].

In Fig. 3(a) we plot the renormalized filling factor $n/n_s$ as a function of chemical potential $\mu$ in a WSe$_2$/WS$_2$ heterobilayer at a twist angle $\theta = 3°$ with different dielectric constants. At low fillings, the charge is always localized at the $MM$ spots. As we increase the filling, more holes will be accumulated and the repulsive interaction renormalizes the charge distribution to make it more homogeneous. Near half filling $n = \frac{1}{2}n_s$, when the interaction is weak, the charge distribution remains at the $MM$ spots as shown in Fig. 3(b). When the interaction is strong, a charge transfer occurs from the $MM$ to $MX$ spots and the corresponding charge distribution is shown in Fig. 3(c).

To go beyond the mean-field approximation, in the following we provide a theoretical description of the charge-transfer physics in a TMD heterobilayer with a sufficiently large $L_{\rm M}$, where the moiré bandwidth $W$ is small compared to the moiré potential $V_0$.

*Tight-binding limit.* We first introduce the moiré kinetic energy as $E_0 \equiv (2mL_{\rm M}^2)^{-1}$, which increases with the twist angle as $E_0 \propto (\theta^2 + \delta^2)$. When the moiré potential is weak compared with the kinetic term $V_0 \ll E_0$ (nearly free limit), the first and second bands have a negative indirect gap [e.g., Fig. 2(b)]. When the moiré potential is much stronger than the kinetic term $V_0/E_0 \gg 1$ (tight-binding limit), the moiré bands become flat compared with the band gaps $W \ll \Delta$ [e.g., Fig. 2(d)]. All untwisted heterobilayers listed in Table I belong to the tight-binding limit as shown in Fig. 4(a).

In the tight-binding limit, each potential minimum traps a set of local Wannier orbitals. The lowest-energy one is an $s$ orbital, and the next is a $(p_x, p_y)$ doublet. The first moiré band is predominantly formed by $s$ orbitals at the $MM$ spots, which are global potential minima in the parameter range of interest $\phi \in (0, \frac{1}{3}\pi)$. The character of the second moiré band depends on $\phi$. For $\phi \in (0, \frac{1}{6}\pi)$, it comes from $(p_x, p_y)$ orbitals at the
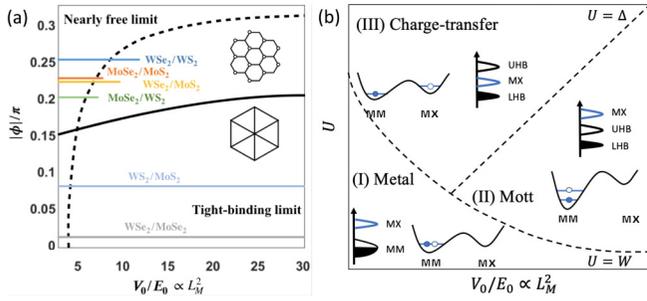
FIG. 4. (a) TMD heterobilayers can be described by different limits and tight-binding models for the first and second moiré bands. Each colored line denotes a TMD bilayer. The nearly free limit and tight-binding limit are separated by the dashed line where $W = \Delta$. (b) Schematic phase diagram at half filling $n = 1$. The solid curve illustrates the landscape of the moiré potential, and the solid and open circles denote occupied holes at $n = 1$ and additional holes above $n = 1$, respectively. In phases (II) and (III), LHB, UHB, and $MX$ denote the lower Hubbard band, upper Hubbard band, and $MX$ anion band, respectively. The densities of states are shown for all phases.

$MM$ spots, and the low-energy physics is well captured by the triangular lattice model [13]. For $\phi \in (\frac{1}{6}\pi, \frac{1}{3}\pi)$ and in a wide range of $V_0$, it comes from $s$ orbitals at the $MX$ spots that are local potential minima (see Fig. 2). The energy difference between the $s$ orbitals in the $MX$ and $MM$ spots defines a charge-transfer gap $\Delta_0 = \varepsilon_{MX} - \varepsilon_{MM}$.

By expanding $V(\boldsymbol{r})$ around a potential minimum, we obtain the characteristic size of $s$ orbitals in the $MM$ and $MX$ spots from the harmonic approximation

$$\psi(r, R) = \frac{1}{\sqrt{\pi}\xi} \exp\left(-\frac{|r - R|^2}{2\xi^2}\right), \quad (5)$$

$$\xi_{MM} = (\cos\phi)^{-1/4}\xi_0, \quad \xi_{MX} = \left[\sin\left(\phi - \frac{1}{6}\pi\right)\right]^{-1/4}\xi_0,$$

$$\xi_0 = (4\pi^2 m V_0)^{-1/4}\sqrt{L_M}, \quad (6)$$

where $\xi_{MX}$ only applies to $\phi \in (\frac{1}{6}\pi, \frac{1}{3}\pi)$. It is important to note that for large $L_M$, $\xi_i \propto \sqrt{L_M}$ is parametrically smaller than the moiré period. Therefore, the local Coulomb repulsion is the largest interaction energy, given by

$$U_i = \frac{e^2}{4\sqrt{2\pi}\epsilon\xi_i} \propto L_M^{-1/2}. \quad (7)$$

with $i = MM, MX$. In contrast, the interaction between nearest neighbors $V'$ is proportional to $1/L_M$ and hence parametrically smaller than $U$.

In Fig. S3 of the Supplemental Material [30] we plot the bandwidth $W$ of the first moiré band and interaction energies $U, V'$ of WSe$_2$/WS$_2$ at different twist angles. While $U, V'$ decrease with $L_M$ in a power-law manner, $W$ is exponentially small in the tight-binding regime. For untwisted WSe$_2$/WS$_2$, we find $L_M = 8.2$ nm, $\xi_{MM} = 2.3$ nm, $\xi_{MX} = 3.0$ nm, $U_{MM} = 764/\epsilon$ meV, $U_{MX} = 594/\epsilon$ meV, $W = 8$ meV, $\Delta E_K = 18$ meV, and $V' = 302/\epsilon$ meV.

Depending on the relative strengths of the interaction energy, bandwidth, and charge-transfer gap, we find three phases at the filling factor $n = 1$, as illustrated in Fig. 4(b).

(I) Metal: $U \ll W$. The system is gapless. Under doping, additional charges are mainly localized at the $MM$ spots with $s$-orbital symmetry.

(II) Mott insulator: $\Delta > U \gg W$. The insulating ground state has one hole per $MM$ spot, and the charge gap is $U$. When doped further, additional charges are mainly localized around the $MM$ spots. In this case, the triangular lattice Hubbard model is a good description [13].

(III) Charge-transfer insulator: $U > \Delta \gg W$. The insulating ground state has one hole per $MM$ spot, but the charge gap is $\Delta$. When further doped, additional charges are mainly localized at the $MX$ spots, thus resulting in charge transfer on the moiré scale as the filling increases.

The insulating gap at half filling inferred from the thermal activation of resistivity is only around 10 meV [15,16], which is significantly smaller than the estimated on-site repulsion $U \sim 128$ meV assuming $\epsilon = 6$. (Note the distance from the sample to metallic gates is 20 nm so that screening has little effect on local repulsion $U$.) However, the measured thermally activated gap [15] is comparable to the charge-transfer gap $\Delta E_K \sim 18$ meV. We thus conclude that the insulating phase at half filling in untwisted WSe$_2$/WS$_2$ is likely a charge-transfer insulator, rather than a Mott-Hubbard insulator.

In order to capture the physics of charge transfer between the $MM$ and $MX$ spots, we introduce an extended Hubbard model on the honeycomb lattice,

$$H = \frac{\Delta}{2}\sum_i (-)^i c_i^\dagger c_i - t\sum_{\langle ij \rangle}(c_i^\dagger c_j + \text{H.c.})$$
$$+ \sum_{ij} V_{ij} n_i n_j, \quad (8)$$

where $c_i = \{c_{i\uparrow}, c_{i\downarrow}\}^T$ denotes $s$-orbital holes, $(-)^i = \pm$ for $i = MX$ ($MM$) spots, and $t$ denotes hopping. $V_{ij}$ is the Coulomb repulsion between $s$ orbitals at sites $i$ and $j$. When there is strong screening from the metallic gates, interactions decay rapidly with the distance between sites.

At the long-wavelength limit $L_M = 8.2$ nm, the kinetic energy is vanishing small compared to local repulsion ($t/U_{MM} < 1/20$ at $L_M = 8.2$ nm) and can be neglected. Within the extended Hubbard model for filling $n = 1$, we further calculate the self-energy of the additional hole filling to the $MM$ site as $E_{MM} = U_{MM} + \sum_{j \in MM} V_{ij}$ with $i \in MM$, and the $MX$ site as $E_{MX} = \Delta + \sum_{j \in MM} V_{ij}$ with $i \in MX$. With moiré wavelength $L_M = 8.2$ nm and gate distance $d = L_M$ [31], we find that adding a hole to the $MX$ site costs much lower energy than adding to the $MM$ site ($E_{MM} = 145$ meV, $E_{MX} = 65$ meV), which is the direct evidence for the charge-transfer insulator in the WSe$_2$/WS$_2$ heterobilayer system.

At temperatures below the charge gap, double occupancy is strongly suppressed by the on-site repulsion $U$. For the triangular lattice Hubbard model, the low-energy physics is described by the $t$-$J$ model [32,33] with hopping $t$ and the antiferromagnetic superexchange interaction $J = 4t^2/U > 0$ between nearest neighbors. Magnetic susceptibility as a function of doping at various temperatures is shown in the Supplemental Material [30]. For charge-transfer insulators such as WSe$_2$/WS$_2$ described by the honeycomb lattice model in Eq. (8), their magnetic properties call for future study.

In real space, the interaction-induced, filling-dependent charge transfer leads to a significant change of charge distribution on the scale of 10 nm, which can be detected by scanning tunneling spectroscopy (STS). In the energy domain, charge transfer affects the band structure on a scale of 10 meV, which may be detected in angle-resolved photoemission spectroscopy and infrared optical conductivity measurements. The extended Hubbard model in a honeycomb lattice has also been realized with cold atoms in an optical lattice [34–38]. In a graphene-based system, the kinetic energy and repulsion are at the eV level, but the tunability is quite limited and it is not possible to have the potential difference between two sites, which is essential for the charge-transfer physics described in this work. However, in cold-atom systems, the lowest accessible temperature at present is on the order of hopping $t$, which is much higher than the exchange interaction $J$ [39]. In the TMD heterobilayer $WSe_2/WS_2$, the exchange energy is around $J \sim 0.05$ meV and can be obtained from the Curie-Weiss fit of temperature-dependent magnetic susceptibility [15].

In conclusion, we present a theory that maps a long-period moiré system onto an atomic crystal with a cation and anion and studies the correlated insulating behavior. We find that the interplay between the moiré potential and interaction strength gives rise to a charge-transfer insulator in TMD heterobilayers, and opens the possibility for different electronic states upon doping [31].

[1] Y. Cao, V. Fatemi, A. Demir, S. Fang, S. L. Tomarken, J. Y. Luo, J. D. Sanchez-Yamagishi, K. Watanabe, T. Taniguchi, E. Kaxiras *et al.*, Nature (London) **556**, 80 (2018).

[2] Y. Cao, V. Fatemi, S. Fang, K. Watanabe, T. Taniguchi, E. Kaxiras, and P. Jarillo-Herrero, Nature (London) **556**, 43 (2018).

[3] G. Chen, L. Jiang, S. Wu, B. Lyu, H. Li, B. L. Chittari, K. Watanabe, T. Taniguchi, Z. Shi, J. Jung *et al.*, Nat. Phys. **15**, 237 (2019).

[4] G. Chen, A. L. Sharpe, P. Gallagher, I. T. Rosen, E. J. Fox, L. Jiang, B. Lyu, H. Li, K. Watanabe, T. Taniguchi *et al.*, Nature (London) **572**, 215 (2019).

[5] R. Bistritzer and A. H. MacDonald, Proc. Natl. Acad. Sci. USA **108**, 12233 (2011).

[6] N. N. T. Nam and M. Koshino, Phys. Rev. B **96**, 075311 (2017).

[7] M. Koshino, N. F. Q. Yuan, T. Koretsune, M. Ochi, K. Kuroki, and L. Fu, Phys. Rev. X **8**, 031087 (2018).

[8] S. Carr, S. Fang, Z. Zhu, and E. Kaxiras, Phys. Rev. Res. **1**, 013001 (2019).

[9] H. Yoo, R. Engelke, S. Carr, S. Fang, K. Zhang, P. Cazeaux, S. H. Sung, R. Hovden, A. W. Tsen, T. Taniguchi *et al.*, Nat. Mater. **18**, 448 (2019).

[10] K. Uchida, S. Furuya, J.-I. Iwata, and A. Oshiyama, Phys. Rev. B **90**, 155451 (2014).

[11] M. Van Wijk, A. Schuring, M. Katsnelson, and A. Fasolino, 2D Mater. **2**, 034010 (2015).

[12] Z. Bi, N. F. Q. Yuan, and L. Fu, Phys. Rev. B **100**, 035448 (2019).

[13] F. Wu, T. Lovorn, E. Tutuc, and A. H. MacDonald, Phys. Rev. Lett. **121**, 026402 (2018).

[14] F. Wu, T. Lovorn, E. Tutuc, I. Martin, and A. H. MacDonald, Phys. Rev. Lett. **122**, 086402 (2019).

[15] Y. Tang, L. Li, T. Li, Y. Xu, S. Liu, K. Barmak, K. Watanabe, T. Taniguchi, A. H. MacDonald, J. Shan *et al.*, Nature (London) **579**, 353 (2020).

[16] E. C. Regan, D. Wang, C. Jin, M. I. B. Utama, B. Gao, X. Wei, S. Zhao, W. Zhao, Z. Zhang, K. Yumigeta *et al.*, Nature (London) **579**, 359 (2020).

[17] J. Hubbard, Proc. R. Soc. London, Ser. A **276**, 238 (1963).

[18] J. Zaanen, G. A. Sawatzky, and J. W. Allen, Phys. Rev. Lett. **55**, 418 (1985).

[19] L. Rademaker and P. Mellado, Phys. Rev. B **98**, 235158 (2018).

[20] L. Rademaker, D. A. Abanin, and P. Mellado, Phys. Rev. B **100**, 205114 (2019).

[21] F. Guinea and N. R. Walet, Proc. Natl. Acad. Sci. USA **115**, 13174 (2018).

[22] C. Zhang, C.-P. Chuu, X. Ren, M.-Y. Li, L.-J. Li, C. Jin, M.-Y. Chou, and C.-K. Shih, Sci. Adv. **3**, e1601459 (2017).

[23] D. Xiao, G.-B. Liu, W. Feng, X. Xu, and W. Yao, Phys. Rev. Lett. **108**, 196802 (2012).

[24] M. H. Naik and M. Jain, Phys. Rev. Lett. **121**, 266401 (2018).

[25] L. Xian, M. Claassen, D. Kiese, M. M. Scherer, S. Trebst, D. M. Kennes, and A. Rubio, arXiv:2004.02964.

[26] G. Kresse and J. Furthmüller, Comput. Mater. Sci. **6**, 15 (1996).

[27] J. P. Perdew, K. Burke, and M. Ernzerhof, Phys. Rev. Lett. **77**, 3865 (1996).

[28] J. Klimeš, D. R. Bowler, and A. Michaelides, Phys. Rev. B **83**, 195131 (2011).

[29] T. Cea, N. R. Waler, and F. Guinea, Phys. Rev. B **100**, 205113 (2019).

[30] See Supplemental Material at http://link.aps.org/supplemental/10.1103/PhysRevB.102.201115 for the construction of commensurate structures, details of the *ab initio* calculation and parameter fitting, and magnetic properties.

[31] K. Slagle and L. Fu, arXiv:2003.13690.

[32] J. Spalek, Acta Phys. Pol., A **111**, 409 (2007).

[33] P. A. Lee, N. Nagaosa, and X.-G. Wen, Rev. Mod. Phys. **78**, 17 (2006).

[34] D. Jaksch, C. Bruder, J. I. Cirac, C. W. Gardiner, and P. Zoller, Phys. Rev. Lett. **81**, 3108 (1998).

[35] W. Hofstetter, J. I. Cirac, P. Zoller, E. Demler, and M. D. Lukin, Phys. Rev. Lett. **89**, 220407 (2002).

[36] M. Greiner, O. Mandel, T. Esslinger, T. W. Hänsch, and I. Bloch, Nature (London) **415**, 39 (2002).

[37] N. Gemelke, X. Zhang, C.-L. Hung, and C. Chin, Nature (London) **460**, 995 (2009).

[38] P. Soltan-Panahi, J. Struck, P. Hauke, A. Bick, W. Plenkers, G. Meineke, C. Becker, P. Windpassinger, M. Lewenstein, and K. Sengstock, Nat. Phys. **7**, 434 (2011).

[39] A. Mazurenko, C. S. Chiu, G. Ji, M. F. Parsons, M. Kanász-Nagy, R. Schmidt, F. Grusdt, E. Demler, D. Greif, and M. Greiner, Nature (London) **545**, 462 (2017).